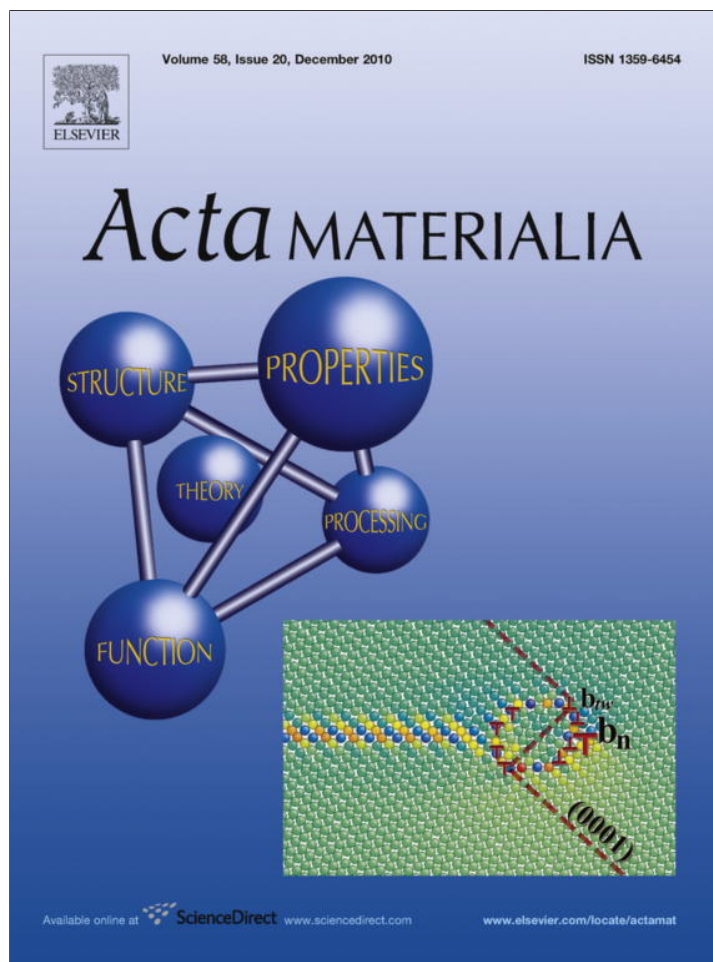


Provided for non-commercial research and education use.
Not for reproduction, distribution or commercial use.



This article appeared in a journal published by Elsevier. The attached copy is furnished to the author for internal non-commercial research and education use, including for instruction at the authors institution and sharing with colleagues.

Other uses, including reproduction and distribution, or selling or licensing copies, or posting to personal, institutional or third party websites are prohibited.

In most cases authors are permitted to post their version of the article (e.g. in Word or Tex form) to their personal website or institutional repository. Authors requiring further information regarding Elsevier's archiving and manuscript policies are encouraged to visit:

<http://www.elsevier.com/copyright>



Orientation dependence of local lattice rotations at precipitates: Example of κ -Fe₃AlC carbides in a Fe₃Al-based alloy

Satoru Kobayashi^{a,*}, Claudio Zambaldi^b, Dierk Raabe^b

^a Osaka Center for Industrial Materials Research, Institute for Materials Research, Tohoku University, 1-1 Gakuen-cho, Naka-ku, Sakai, Osaka 599-8531, Japan

^b Max-Planck-Institut für Eisenforschung, Max-Planck-Str. 1, 40237 Düsseldorf, Germany

Received 5 October 2009; received in revised form 19 August 2010; accepted 20 August 2010

Available online 28 September 2010

Abstract

Local lattice rotations and in-grain orientation gradients at κ precipitates in matrix grains with orientations near the 45° rotated cube $\{0\ 0\ 1\}\langle 1\ 1\ 0\rangle$ (RC) and the γ -fiber components $\{1\ 1\ 1\}\langle 1\ 1\ 2\rangle$ were investigated in a Fe₃Al alloy warm-rolled to reductions of between 10% and 60%. Near-RC grains showed larger local lattice rotations at precipitates than γ -fiber grains. In RC-oriented grains the local lattice rotations about the transverse direction (TD) were dominant at low reductions, but rotations about the rolling direction (RD) also occurred at higher strains. In the γ -fiber grains the axes of the in-grain lattice rotations were scattered between TD and RD. The rotations around the particles and their orientation dependence were analyzed using 3-D crystal plasticity finite-element simulations of a spherical inclusion in a plane strain deformed matrix of different orientations, namely RC, $\{1\ 1\ 1\}\langle 1\ 1\ 2\rangle$ and $\{1\ 1\ 1\}\langle 0\ 1\ 1\rangle$.

© 2010 Acta Materialia Inc. Published by Elsevier Ltd. All rights reserved.

Keywords: Deformation structure; Texture; EBSD; Iron aluminides

1. Introduction

When crystalline materials are plastically strained the crystal lattice often rotates as locally subdivided units within originally homogeneous grains. These local lattice reorientations, leading to orientational gradients within grains (in-grain orientation gradients, grain fragmentation), are known to depend on the initial grain orientations of the materials with respect to the imposed load [1–3]. The orientation dependence may cause inhomogeneity of local strain hardening and of recrystallization kinetics during annealing, i.e. higher in-grain orientation gradients promote faster recrystallization kinetics. A number of studies on this subject have been published for materials with body-centered cubic (bcc) crystal structure, deformed under near-plane-strain conditions [3–10]. The 45° about the normal direction (ND) rotated cube (RC) texture com-

ponent, $\{100\}\langle 0\ 1\ 1\rangle$, shows in bcc materials very weak in-grain orientation gradients even after large plane-strain deformation and very sluggish recrystallization kinetics, whereas orientations that belong to the γ -fiber texture component, $\{1\ 1\ 1\}$ //normal direction (ND), typically reveal much stronger in-grain orientation gradients and, hence, faster recrystallization kinetics when exposed to a heat treatment. Early studies on this subject were made by Hu [4,5] in Fe–Si single crystal and by Dillamore [6,7] in pure Fe. Recent works using finite-element methods and electron backscatter diffraction (EBSD) have provided detailed data about in-grain orientation gradients and their consequences in the different texture components [3,8–12].

Fe₃Al-based alloys exhibit bcc-related crystallographic structures, i.e. bcc, B2 and D0₃ with decreasing temperature. The alloys typically show similar orientation dependence of the texture evolution and deformation/recrystallization behavior as commonly observed in single-phase bcc materials [13–20]. It was found in a Fe₃Al-based alloy that a strong RC and γ -fiber texture was devel-

* Corresponding author.

E-mail address: kobayashi@imr.tohoku.ac.jp (S. Kobayashi).

oped during warm rolling. Further, it was observed that γ -fiber grains recrystallized, but near-RC grains mainly recovered even after long annealing treatment.

As a consequent next step in the further alloy and microstructure development strategy we introduced coarse particles into the matrix to promote local deformation inhomogeneities in the form of lattice rotations at the precipitates during deformation [21–26]. The goal of this microstructure modification consists in promoting recrystallization nucleation during annealing in order to achieve grain refinement. In our current study, we find in warm-rolled samples that RC-oriented grains indeed show larger in-grain local lattice rotations at κ -Fe₃AlC carbide precipitates than γ -fiber oriented grains [26]. This finding describes an opposite trend when compared to the orientation dependence of reorientation and grain fragmentation observed in particle-free bcc-based materials described above [3–20].

Local lattice rotations at particles (particle-affected deformation zones) have been intensively investigated within several main texture components especially in Al alloys [27–35], but experimental evidence showing strong orientation dependence of the local lattice rotations at precipitates has not yet been reported. As a theoretical approach along this line Gottstein's group recently conducted quantitative coupled finite-element modeling–texture simulations on the orientation evolution around hard particles [35].

In view of our recent experimental findings, the purpose of this paper is to investigate the orientation dependence of local lattice rotations and in-grain orientation gradients at κ precipitates in two main stable matrix orientations, $\{001\}\langle 110\rangle$ and $\{111\}\langle 112\rangle$, in a warm-rolled Fe₃Al alloy. The term “stability” here refers to the reorientation behavior of the grains without the presence of particles under plane-strain loading. We show that the orientation dependence of the deformation field around particles in otherwise stable grains creates locally highly instable situations that locally lead to high reorientation values.

2. Experimental procedures

The nominal composition of the alloy studied was Fe–26.4Al–1.2C–1.0Mo (at.%). This alloy was prepared from 3 N purity iron, 4 N aluminum, 3 N chromium, 4 N molybdenum and 3 N carbon as a 2 kg ingot by induction melting in an argon atmosphere. In this alloy, the κ -Fe₃AlC carbide phase is precipitated within the bcc matrix below ~ 1150 °C, and the bcc matrix orders to B2 and to D0₃ at ~ 900 and ~ 550 °C, respectively [26].

The ingot was hot rolled to a thickness of 1.7 mm. The plate was cut to a size of $10 \times 1.7 \times 50$ mm³ and subsequently heat treated at 1200 °C in the bcc single-phase field for 15 min followed by air cooling. The air-cooled plate was warm-rolled under lubrication using a furnace temperature of 700 °C at which the matrix phase is B2 ordered. The reduction per pass was about 5%. Microstructures

and crystal orientations were analyzed in the samples rolled to reductions of 10%, 25%, 40%, 50% and 60%. From each warm-rolled slab a sample was cut for microstructure analysis. The RD–ND planes were ground and mechanically polished down to 1 μ m Al₂O₃ followed by electropolishing in a solution of 93% ethanol + 7% perchloric acid.

Orientations of the matrix grains in the warm-rolled samples were analyzed using TSL software based on the analysis of EBSD patterns in a field emission scanning electron microscope (FESEM). The step size for the analysis in the EBSD measurements was 0.5 μ m. The microstructure of the samples was observed using optical microscope and a backscattered electron (BSE) detector in the FESEM.

3. Results and discussion

3.1. Matrix grain size, orientation and morphology of κ precipitates

Fig. 1 shows an optical micrograph and an EBSD inverse pole figure (IPF) map of the RD–ND section of the entire rolled sample after a reduction of 10%. It can be seen that rod-like κ precipitates are distributed in ~ 1 mm sized large grains. The large grain size was attributed to the heat treatment at 1200 °C in the bcc single-phase field. A preliminary EBSD measurement with a coarse step size (5 μ m) revealed that grains with orientations near RC and γ -fiber texture components exist near the center position of the sample. Fig. 2a shows an IPF map taken at 0.5 μ m step size from the enclosed area in Fig. 1b. The matrix orientations, determined in regions a few tens of micrometers away from the κ precipitates, were (1 2 23)[17 –20 1] and (18 13 15)[5 –15 7] in the RC and γ -fiber grain, respectively. The areas that were at least 10 μ m away from the grain boundaries, such as the enclosed areas shown in Fig. 2a, were used for the investigation of local lattice rotations at κ precipitates in order to avoid superimposed constraints of a grain boundary. Table 1 lists the matrix host orientations in which the local orientations were analyzed at each rolling reduction level.

Fig. 2b shows a BSE image corresponding to Fig. 2a. It shows that the rod-like κ precipitates assume different directions. An EBSD analysis revealed that the longitudinal axes of the κ rods are parallel to the $\langle 112\rangle$ directions in the matrix. The volume fraction and the diameter of κ rods were measured as $\sim 12\%$ and 3–7 μ m, respectively.

3.2. Local lattice rotations and orientation gradients at κ precipitates

Although local lattice rotations at the precipitates can be recognized qualitatively in Fig. 2a they were also quantitatively analyzed using the Grain Reference Orientation Deviation (GROD) function. This tool reveals the angular deviation of each point relative to a given reference orientation, e.g. a point representing the stable grain interior far

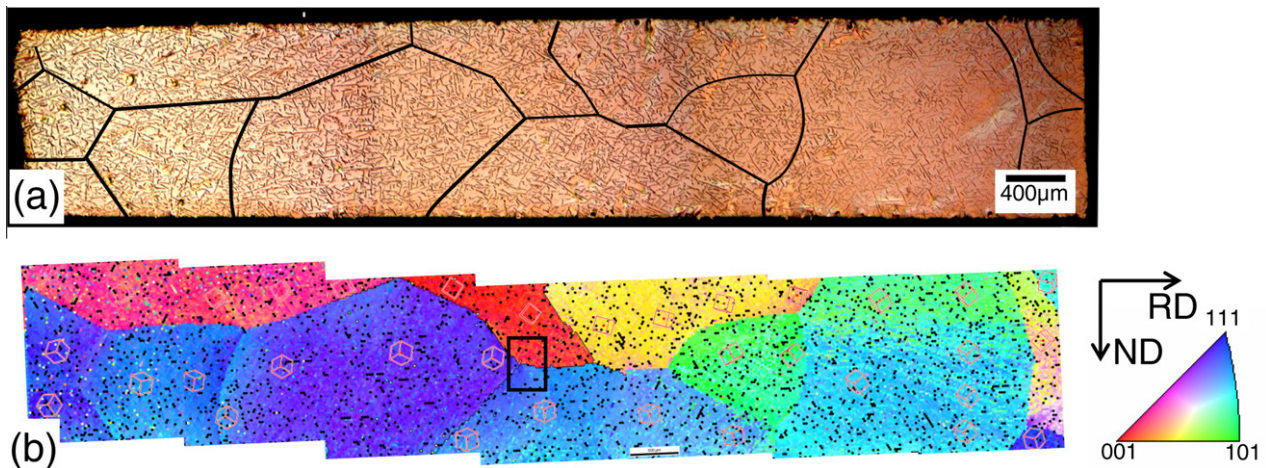


Fig. 1. The RD–ND section of the entire sample rolled to a thickness reduction of 10%: (a) optical micrograph; (b) EBSD inverse pole figure (IPF) map. Grain boundaries ($>15^\circ$) are drawn by solid lines in (a). (For interpretation of the references to color in this figure legend, the reader is referred to the web version of this article.)

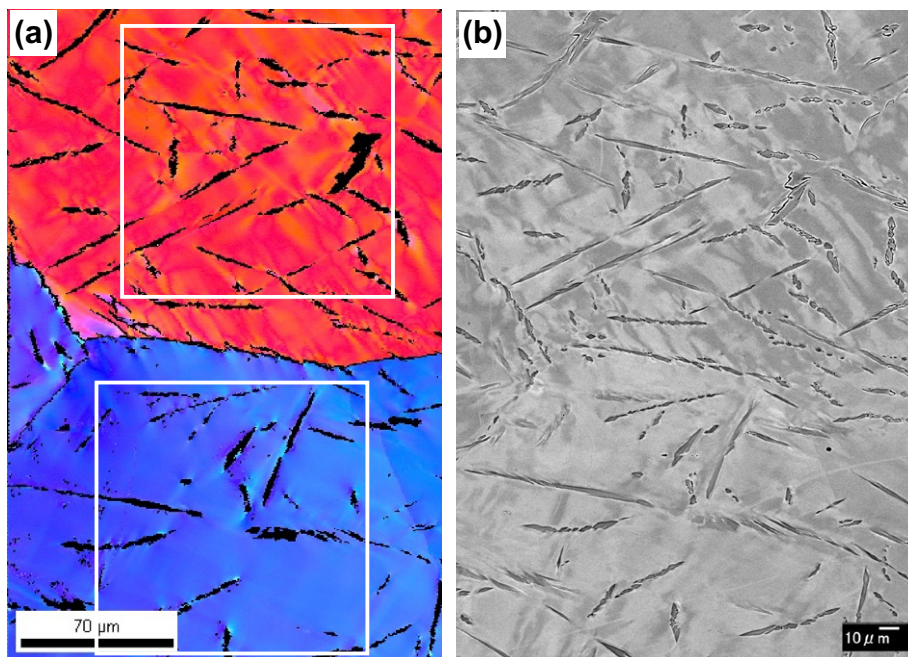


Fig. 2. (a) An EBSD IPF map and (b) a BSE image obtained from the enclosed area in Fig. 1b. The color index for the EBSD map (a) is indicated in Fig. 1. The κ precipitates are colored by black in (a). (For interpretation of the references to color in this figure legend, the reader is referred to the web version of this article.)

away from the precipitate interface. The tool is available in the TSL-OIM software. Fig. 3a and b shows such GROD maps in which the color code given in the index reveals those areas that are highly misorientated by more than 15° with respect to the average matrix orientation. The GROD maps depicted in Fig. 3 are given for the squared areas in Fig. 2a. It can be seen that the highly misorientated areas are formed frequently at the tips of κ precipitates in RC-oriented grain (Fig. 3a), while such zones occur less frequently in γ -fiber oriented grains (Fig. 3b). At a sheet thickness reduction of 60%, the frequency of the misorientated areas increases and the maximum local misorienta-

tion angles reach values as large as $45\text{--}60^\circ$ in the RC grain (Fig. 3c). Highly misorientated areas are visible also in the γ -fiber grain, but their frequency is far below that observed in RC-oriented grains. In addition, it can be seen in both types of grains that smaller local lattice rotations tend to occur at κ rods the longitudinal axes of which are inclined $15\text{--}30^\circ$ from the RD within the ND–RD plane.

Fig. 4 shows the change in the fraction of highly misorientated areas in the two matrix orientations as a function of the rolling reduction. At all rolling reductions the fraction of the areas and the degree of the maximum misorientations are higher in the RC orientations than in the γ -fiber

Table 1

The orientations of matrix grains in which local lattice rotations at κ precipitates were analyzed. Each orientation was taken from the average orientation of matrix remote from the precipitates. The deviation angles from the RC or the (1 1 1)(1 1 2) orientation are also listed.

Rolling reduction	Component	$(hkl)[uvw]$	Euler angles (Bunge)			Deviation angle (°)
			φ_1	Φ	φ_2	
10	RC	(1 2 23)[17 -20 1]	5.1	4.0	45.0	7.1
25	RC	(0 0 1)[11 -19 0]	14.9	0.0	45.0	14.9
40	RC	(0 0 1)[16 -19 0]	4.9	0.0	45.0	4.9
50	RC	(0 0 1)[11 -19 0]	14.9	0.0	45.0	14.9
60	RC	(0 0 1)[11 13 0]	85.3	0.0	45.0	4.7
10	GF	(18 13 15)[5 -15 7]	30.0	54.9	55.0	10.0
25	GF	(24 19 17)[2 -7 5]	44.5	60.0	50.0	14.5
40	GF	(21 23 31)[5 -14 7]	35.0	45.0	45.0	10.8
40	GF	(22 23 40)[28 -32 3]	4.0	40.0	45.0	15.5 ^a
50	GF	(10 9 8)[7 -22 16]	40.0	60.0	50.0	14.4
50	GF	(10 8 9)[5 -13 6]	30.0	54.9	50.0	5.0
60	GF	(6 6 5)[9 -19 12]	34.9	59.8	45.0	7.0

^a The deviation angle from {1 1 1}<1 1 0>.

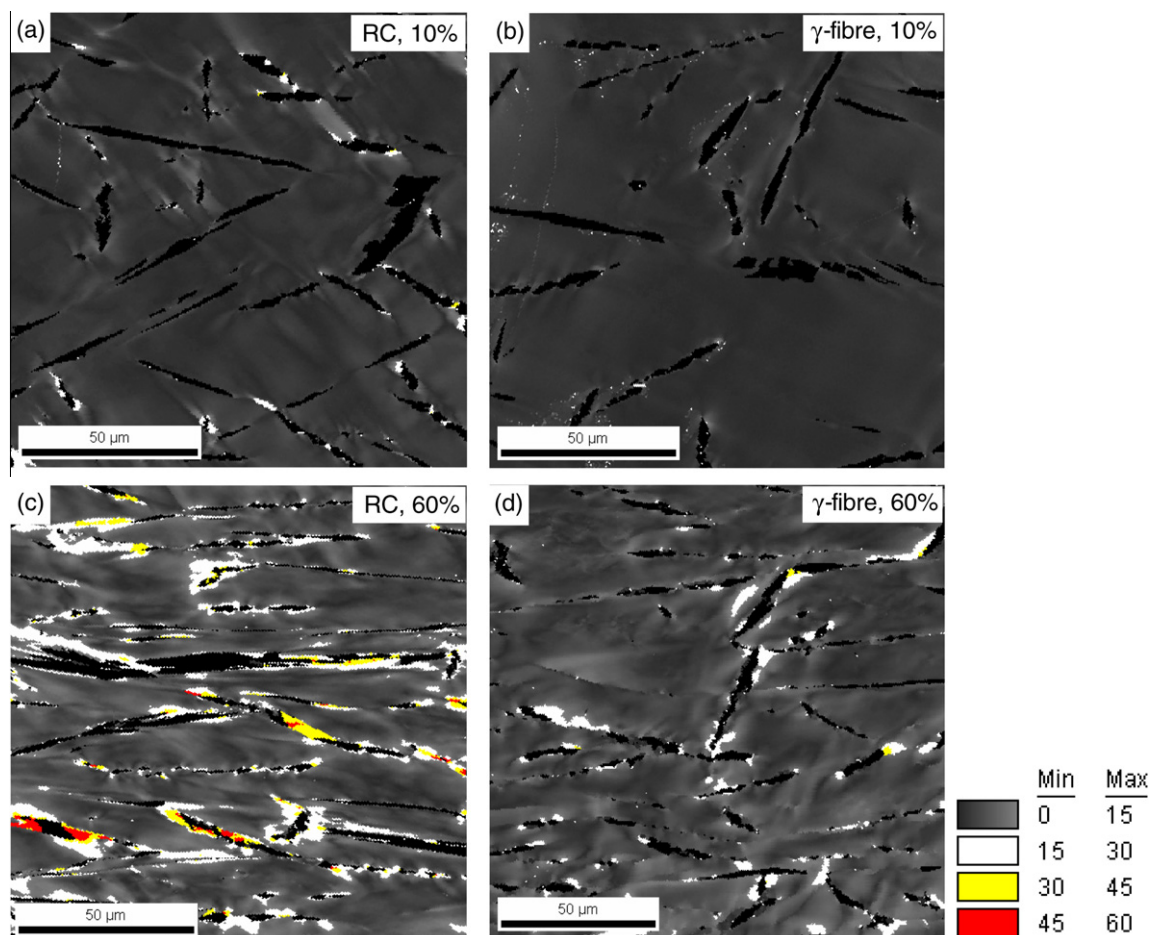


Fig. 3. EBSD Grain Reference Orientation Deviation (GROD) maps obtained from samples warm-rolled to a reduction of 10% (a and b) and 60% (c and d) in the RC-oriented grains (a and c) and γ -fiber-oriented grains (b and d). The areas misoriented by more than 15° with respect to the averaged matrix grain are indicated by the colors. (For interpretation of the references to color in this figure legend, the reader is referred to the web version of this article.)

orientation. This result indicates a higher susceptibility to large local lattice rotations and orientation split-up in the RC grains than in γ -fiber grains in those regions that are affected by the precipitates. Fig. 5 displays details of the

local lattice rotations and orientation gradients at the κ precipitates in terms of the corresponding GROD maps. The following common features are observed regardless of the matrix orientation: (1) The morphology and loca-

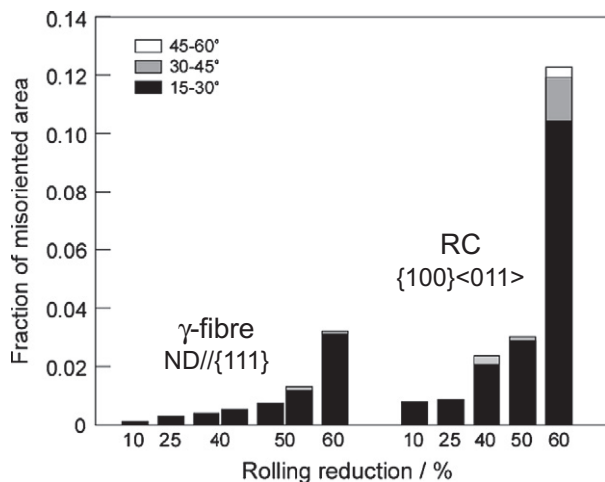


Fig. 4. Change with rolling reduction in the fraction of locally misoriented areas with respect to the average matrix orientations. The misorientation angles are divided into the three ranges: 15–30°, 30–45° and 45–60°. RC: 45° rotated cube orientation.

tions of locally highly misoriented areas are dependent on the alignment of the κ rods with respect to the loading reference coordinate system; (2) the magnitude of the local misorientation accumulation in front of the precipitates increases with decreasing spacing to the precipitate interfaces; (3) there are several misoriented zones around each precipitate. These zones assume a symmetrical arrangement (e.g. A and C, B and D in Fig. 5a shows similar lattice rotations).

The increase in the local misorientations when approaching the particle interfaces [23,28,33,34] and the occurrence of several misoriented zones and their symmetrical arrangement around a particle were reported previously in the literatures [30–32]. Accumulated misorientation profiles relative to matrix orientations were taken along the paths indicated by the lines in Fig. 5, and are quantified in Fig. 6. It can be recognized that the orientation gradients increase when approaching the precipitates in all cases. The values of the maximum occurring orientation gradients, indicated in the figure, appeared to be independent of the matrix orientations, and rather dependent on the position of the inspected zones around the κ precipitates.

3.3. Rotation axes and signs of local lattice rotations at the precipitates

Fig. 7 shows the local lattice rotation axes observed before the κ precipitates in each matrix grain investigated in the warm-rolled samples. The axes are stereographically projected relative to the material coordinate system using plane symmetry as a reference frame. Although the rotation axes are scattered, the following tendencies can be recognized. (1) In the RC-oriented grains the rotation axes are concentrated near the TD-axis of the matrix phase at low rolling reductions (see Fig. 7a–c). (2) The axes are, however, scattered from TD towards RD at high thickness

reductions (Fig. 7d and e). Note that rotation axes close to RD occur frequently in the sample that is rolled to a thickness reduction of 60% (Fig. 7e). (3) In the γ -fiber grains the rotation axes are rather scattered from TD to near RD at all rolling reductions (Fig. 7f–j).

The local lattice rotations about a crystallographic direction near TD or about TD are considered to accommodate deformation incompatibilities between the matrix and the second-phase hard particles under plane-strain loading [27,28,36]. As will be discussed below in more detail, the rotation axis is closely connected to the skew-symmetric portion of the velocity gradient that is created by the active slip system in the shear zones before the precipitates. The reason for the local rotation about RD is not well understood, but the rotations were frequently observed between two κ rods which had long axes parallel to RD. Since the κ rods gradually rotate with increasing rolling reduction towards the rolling plane and RD, such rotations would naturally more often occur at high rolling reductions.

Fig. 8 shows the signs of the local lattice rotations about TD in a RC-oriented grain at a thickness reduction of 10%. The matrix orientations visualized in the figure reveal that two types of rotation branches exist. Clockwise rotations are observed on one diagonal line at the precipitate (indicated by B and D in Fig. 8) and anticlockwise rotations occur on the other diagonal line in regions A and C. Such rotation branches with a change in sign (i.e. in rotation sense) were in all grains observed regardless of the matrix orientation without any exception. Local lattice rotations at particles similar to the present case were reported in a metastable $\{0\ 1\ 1\}\langle 1\ 0\ 0\rangle$ orientation in a face-centered cubic (fcc) crystal under plane-strain deformation [31]. They were explained in terms of a “slip shadowing” model in which the presence of a particle prevents the activation of a certain slip system.

Fig. 9 illustrates the model in which the active slip systems S1 and S2 are restricted by the particle under externally imposed plane-strain loading. In regions such as A and C, slip on slip system S1 will be suppressed by the particle. Slip on system S2 will cause a clockwise crystal rotation. An anticlockwise rotation, in contrast, will occur in regions B and D due to the restriction of slip on the S2 system. The resulting rotation branches, however, do not agree with the ones observed in the present study (compare Figs. 9 and 8).

3.4. Kinematic interpretation of the orientation dependence of local lattice rotations at precipitates

The high stability of RC grains under plane-strain deformation is due to the symmetric kinematics of the active slip systems, i.e. two sets of geometrically compatible $\{1\ 1\ 2\}\langle 1\ 1\ 1\rangle$ and/or $\{1\ 1\ 0\}\langle 1\ 1\ 1\rangle$ slip systems prevail during deformation [3,4,9,10]. The crystallographic lattice spin resulting from the skew-symmetric contribution of these equally stressed systems is in the RC orientation bal-

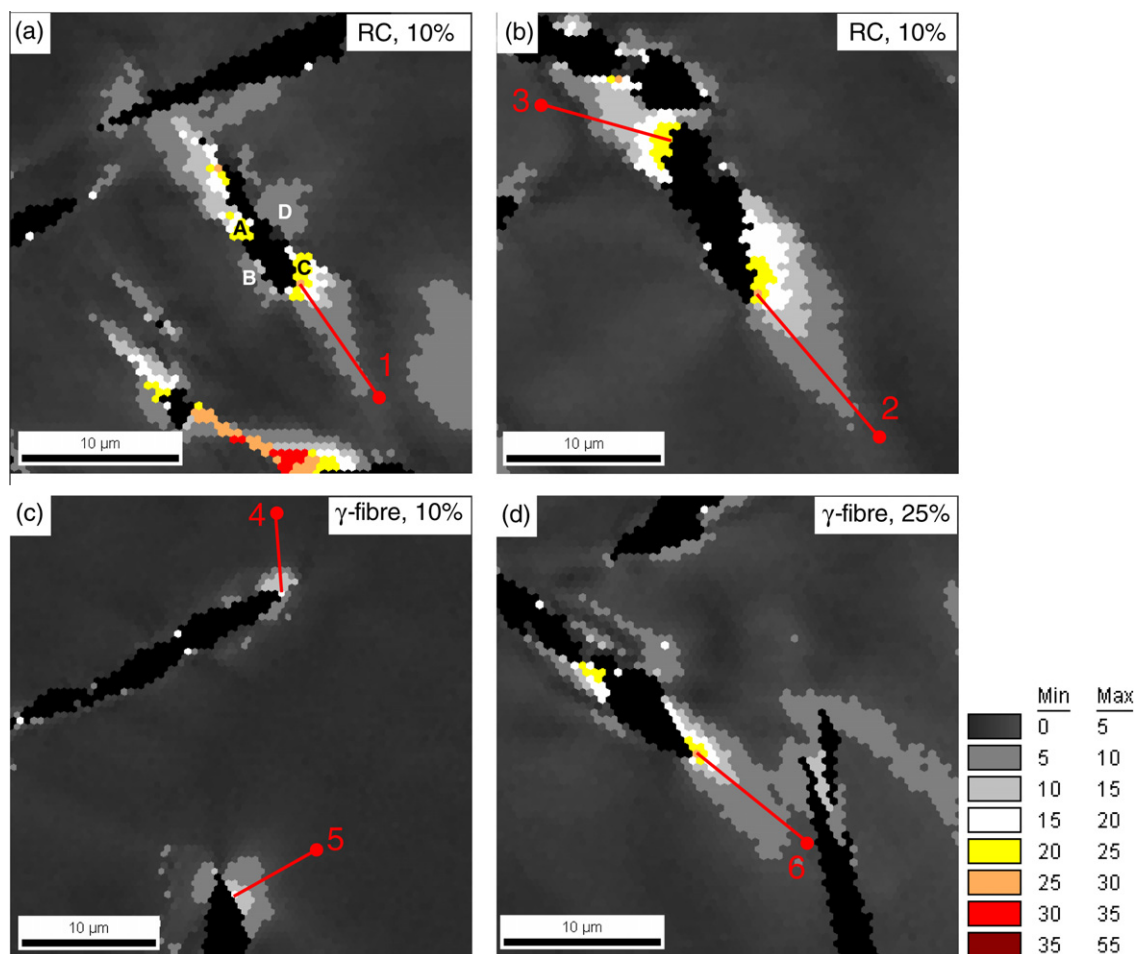


Fig. 5. EBSD GROD maps obtained from the samples warm-rolled to reductions of 10% (a–c) and 25% (d), showing the morphology of locally misoriented areas and orientation gradients at κ precipitates in RC-oriented grains (a and b) and γ -fiber-oriented grains (c and d).

anced out so that the net reorientation is practically zero [3].

The presence of a second-phase particle within the RC grain interior matrix, however, changes the plane-strain deformation field into a shear state in its vicinity [28,35]. This change in the local boundary conditions leads to the activation of slip system combinations with a non-vanishing skew-symmetric portion of the velocity gradient. This effect results in a lattice rotation, i.e. an orientation that is stable under plane-strain deformation can be rendered highly unstable when exposed to a (local) shear deformation state [37].

3.5. Crystal plasticity finite-element simulations of the lattice rotation around a spherical inclusion

In order to obtain a more quantitative estimate of the reorientation or instability tendency of the particle-affected regions in the different grains we conducted crystal plasticity finite-element simulations. Only a few simulation studies of the heterogeneous deformation of a crystalline matrix containing a hard particle have been carried out

to date that take into account the crystallographic nature of the deforming matrix. Out of these, the majority was conducted on metals with fcc structure, mainly on Al [35,38,39].

The present simulations were carried out using an elastoviscoplastic crystal plasticity formulation implemented as the hypela2 subroutine of the commercial finite-element system MSC/Marc that was used to solve the non-linear boundary value problem. While the precipitates in the studied material assumed rod-shaped geometries, the finite-element discretization and subsequent deformation simulations were performed for the case of a spherical inclusion to derive more general and symmetric insights of lattice rotation effects at particles in bcc structures. The particle was modeled by a sphere inside a cube. The matrix phase was discretized into 5376 linear hexahedral elements by a structured mesh approach (Fig. 10).

The particle was assigned purely elastic behavior with a Young's modulus of 60 GPa and a Poisson ratio of 0.44, and its diameter was chosen to be 10% of the model side length. This diameter of the inclusion led to a much lower volume fraction of the particle in comparison to the exper-

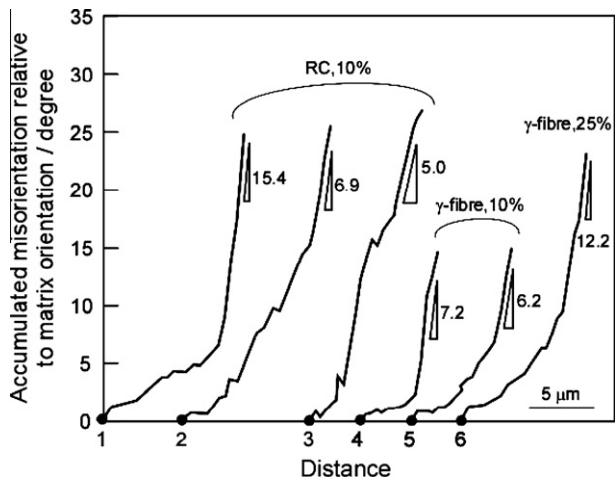


Fig. 6. Accumulated misorientation profiles relative to matrix orientations along the lines 1–6 in Fig. 5. The starting points of the profiles correspond to the numbered dots in Fig. 5. The values of the maximum orientation gradients in degree/ μm are indicated at each profile.

imental situation. The interaction of densely spaced particles is of some importance in the experiments, but this effect lies beyond the scope of the current simulations. In addition, the experimental examples that we chose to compare the predictions with did not show pronounced particle interaction effects.

An overview of the crystal plasticity finite-element method (CPFEM), including the used phenomenological model [40], has recently been given by Roters et al. [41]; hence, a basic introduction into the method is omitted here. The elasto-viscoplastic single-crystal constitutive law used here derives from the model presented by Kalidindi et al. [40] and the simplified constitutive law is given by:

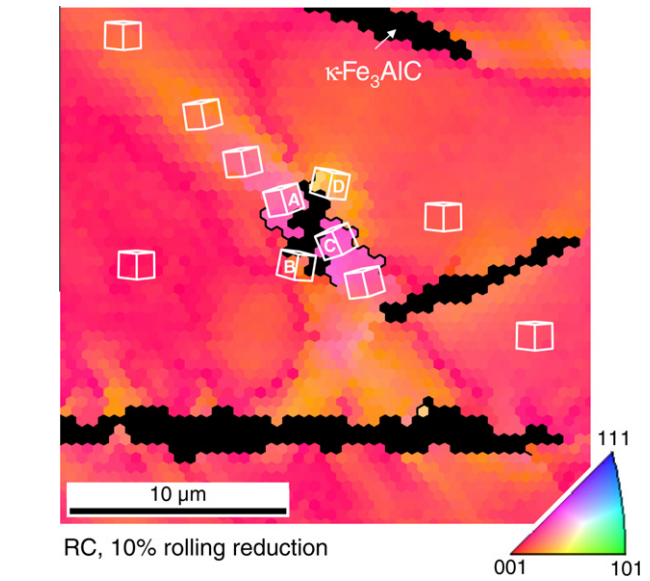


Fig. 8. An EBSD IPF map showing the signs of the local lattice rotations at κ precipitates in a RC grain by schematic unit cells of bcc structure in the sample warm-rolled to a reduction of 10%.

$$\dot{\gamma}^\alpha = \dot{\gamma}_0 \left| \frac{\tau^\alpha}{\tau_{crit}^\alpha} \right|^{1/m} \text{sign}(\tau^\alpha), \quad \text{and}$$

$$\dot{\tau}_{crit}^\alpha = \sum_\beta h_0 \left\{ 1 - \frac{\tau_{crit}^\beta}{\tau_s} \right\}^a |\dot{\gamma}^\beta|$$

with the crystallographic shear rate, $\dot{\gamma}$, and the critical resolved shear stress, τ_{crit} , on slip systems α or β . The relevant parameters that govern the initial strength and the hardening, $\Delta\tau_{crit}^\alpha$, of the individual slip systems are the initial critical shear strength, τ_0 , the saturation shear strength, τ_s , a

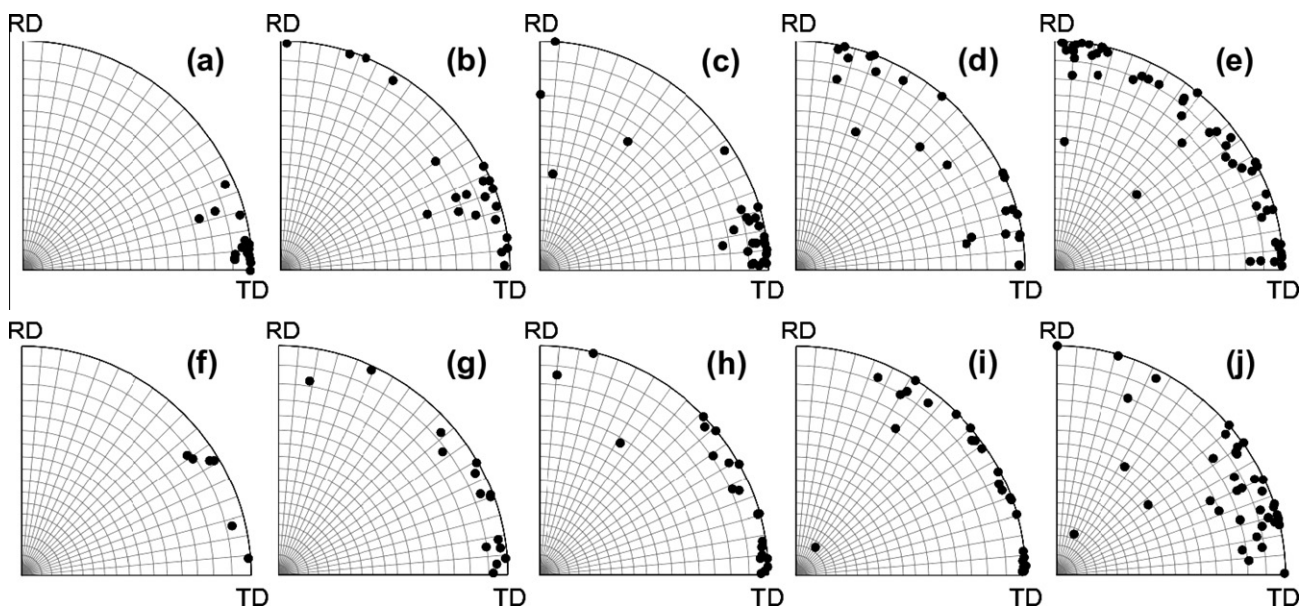


Fig. 7. The axes of local rotations at κ precipitates observed in each sample rolled to a reduction of (a and f) 10%, (b and g) 25%, (c and h) 40%, (d and i) 50% and (e and j) 60% in (a–e) RC grains and (f–j) γ -fiber grains. The axes are stereographically projected on quarter circles based on the material coordinate taking into account rolled sample (orthotropic) symmetry.

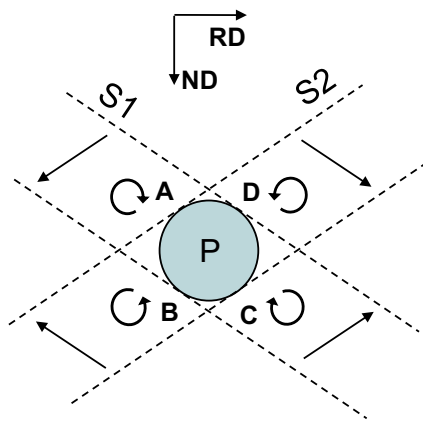


Fig. 9. Schematic illustrations showing local lattice rotations around a particle by slip shadowing model [31]. The arrows depict the original shear directions on the primary slip systems.

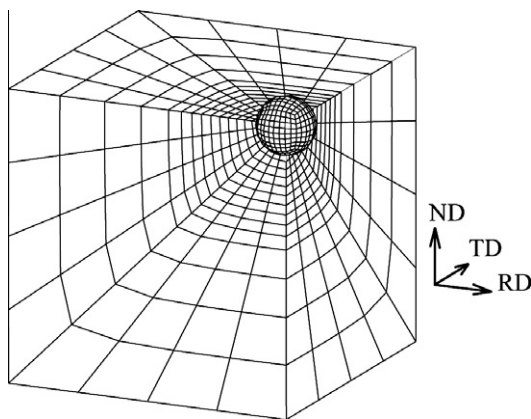


Fig. 10. The structured finite-element mesh containing a spherical particle at the center. The matrix is discretized into 5376 hexahedral elements of which only one-eighth is shown.

factor h_0 , which is influencing the initial self-hardening slope, and a parameter, a , which governs the shape of the self-hardening curve (a was kept constant at a value of 2.5 for all simulations). In addition, the reference shear rate, $\dot{\gamma}$, and the power-law exponent, $1/m$, were kept constant at 0.001 s^{-1} and 20, respectively.

For the slip systems of the B2 structure $12 \{1 1 0\} \langle 1 1 1 \rangle$ and $12 \{1 1 2\} \langle 1 1 1 \rangle$ systems were included. Identical initial slip resistances and self-hardening behavior were assumed for both types of slip. No difference between the strength of the self-hardening and the latent hardening was assumed. Three different matrix orientations were used in the simulations, namely the 45° -ND-rotated cube (RC) and two orientations from the γ -fiber (Table 2).

Different modifications of the plane-strain boundary conditions have been applied: periodic displacement boundary conditions were used on the surface but lead to slightly decreased numerical stability of the finite-element solver when compared to the more rigid flat face boundary conditions. However, the resulting deformation around the particle was virtually unaffected by the choice between

Table 2

The three matrix orientations prescribed in the CPFEM simulations.

Orientation	ND–RD	Bunge Euler angles ($\varphi_1, \Phi, \varphi_2$) ($^\circ$)
Rotated cube (RC)	(0 0 1)[1 -1 0]	(0, 0, 45)
Gamma fiber I	(1 1 1)[-1 -1 2]	(90, 54.74, 45)
Gamma fiber II	(1 1 1)[0 -1 1]	(60, 54.74, 45)

these two types of boundary conditions. Therefore, the flat face boundary conditions were applied to all simulations discussed here. Plane-strain deformation was imposed to a maximum height reduction of 60%, corresponding to a true compressive strain of 0.92. Because of the high mesh distortion around the particle at large deformation, the further evaluation was performed only for strains up to 30% rolling reduction in order to avoid mesh-related misinterpretations.

For all matrix orientations, regions of misoriented material developed around the inclusion with increasing simulated rolling reduction. Fig. 11 gives the lattice rotation away from the initially assigned orientations in the undeformed state. The morphology of the zones of higher lattice rotations were in qualitative agreement with previous 2-D studies on fcc material [38,39]: the lattice rotation is concentrated in inclined zones of misoriented material that originate very close to the particle surface and protrude into the matrix. Also, a significant rigid body rotation of the particle was observed for the $(1 1 1)[-1 -1 2]$ matrix orientation (Fig. 11b). The rotation sense was negative around the TD-axis and the rotation angle was approximately 10° at 30% simulated rolling reduction.

The extension of the rotation zones away from the particle surface was observed to be highly sensitive against the chosen hardening parameters. Parameters representing a low work-hardening behavior ($\tau_s = 12\tau_0$; $h_0 = 4\tau_0$; $a = 2.5$) led to strong confinement of the deformation zones close to the particle surface; in addition, some counter-rotation, i.e. rotation of the crystal lattice in the opposite sense, was observed along the radial direction away from the particle. If higher hardening was assumed ($\tau_s = 10\tau_0$; $h_0 = 20\tau_0$; $a = 2.5$), the rotation sense stabilized and better agreement with the experimentally measured lattice rotations was observed.

For the RC matrix orientation, remote from the particle, two non-coplanar $\{1 1 2\} \langle 1 1 1 \rangle$ slip systems out of the 24 systems were highly active, as discussed in Section 3.4. For both γ -fiber orientations at least three slip systems were significantly activated in the bulk grain. Activation of additional slip systems in the vicinity of the particle was observed for all three matrix orientations.

Fig. 12 compares the experimental and simulated $(1 1 1)$ pole figures at different levels of rolling reduction for all three matrix orientations. Some differences between the analyzed rolling reductions in the experiments (10% and 25%) and between experiments and simulations (40% and 30%) are present but we believe that these have a negligible effect on the validity of our conclusions. For the RC-ori-

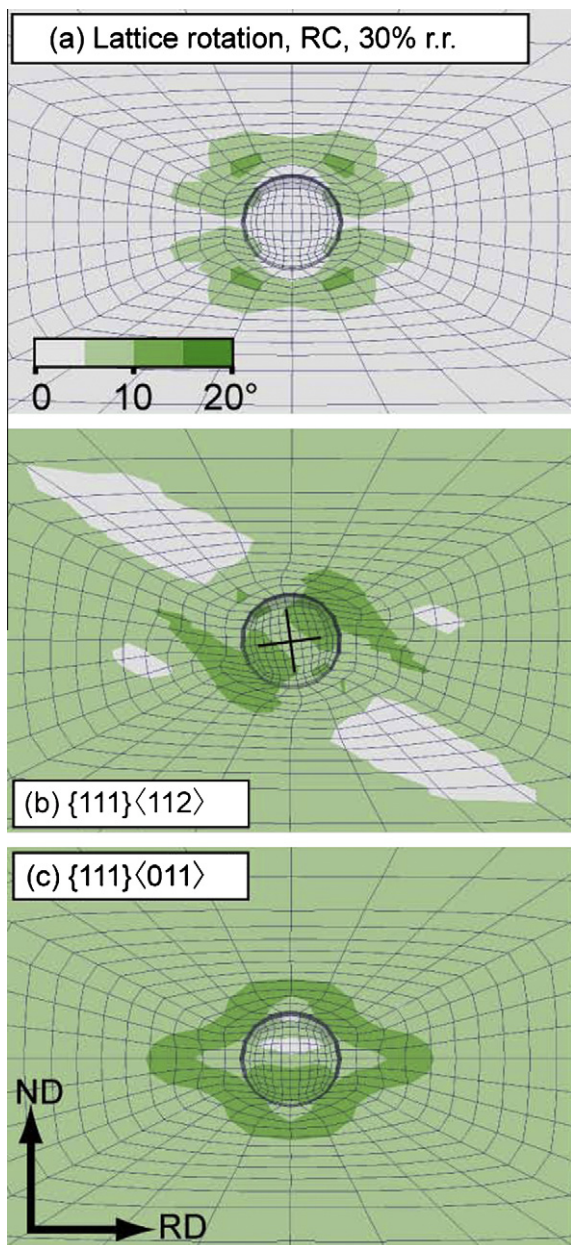


Fig. 11. Lattice rotation away from the initial orientation at 30% simulated rolling reduction. In the case of a matrix with $\langle 112 \rangle$ γ -fiber orientation a rotation of about 10° of the spherical particle is observed.

ented matrix, the experimentally measured TD-rotation was correctly predicted by the simulations. TD-rotations prevailed up to 30% rolling reduction in the simulations while more randomly oriented additional axes were observed in the experiments. For the two γ -fiber orientations, random orientation axes were predicted by the FE simulations, which is in qualitative agreement with the experiments. In summary, considerable orientation spread was predicted with increasing rolling reductions for all three matrix orientations.

Additionally, deformation of the three matrix orientations was simulated without a particle by assigning the bcc constitutive law to the entire volume. The resulting (111) pole figures at 30% rolling reduction are superim-

posed as red data points in Fig. 12(j–l). Very small orientation spread in comparison to the simulations with particle was predicted in all cases. In addition, no significant bulk rotation of the homogeneous RC matrix was observed, in agreement with earlier studies [3]. In contrast, a bulk rotation of 5° and 7° was simulated for the homogeneous $\langle 112 \rangle$ and $\langle 011 \rangle$ γ -fiber orientations, respectively. Identical bulk rotations were found in the simulations with particle. In the experiments, any net rotation in the bulk could not be analyzed because only the orientations in the deformed state were measured and the initial orientations remained unknown.

Fig. 13 shows the simulated lattice rotation around the TD-axis for the RC matrix orientation after 30% rolling reduction. As for this orientation the lattice rotation is almost exclusively taking place around TD, the result is similar to Fig. 11a showing the total lattice rotation, though with additional presentation of the rotation sense. Four large deformation zones and four small deformation zones are formed around the particle in the simulations. The zones exhibit rotation angles of up to around 15° and correspond to those observed in the experiments (cf. to Fig. 8). The sense of local lattice rotations in the deformation zones of the RC matrix simulation shows reasonable agreement with the experimental findings.

The lattice rotation away from the initially assigned orientation is readily available from the CPFEM simulations. Nevertheless, for comparison with the experimentally measured EBSD data, the predicted orientation data should also be presented as GROD maps. It is important to keep in mind the difference between the GROD visualization of in-grain orientation deviations and the rotation away from the initially assigned orientation. The two analysis methods will give similar results only if no net rotation of the bulk occurs. This is approximately the case for the RC matrix orientation. However, for the γ -fiber orientations a bulk rotation of a few degrees away from the starting orientations was observed in the simulations, as mentioned above. Therefore, to analyze the GROD in the same way as for the experimental data, 2-D slices of the simulation results were exported to the TSL-OIM software format to generate GROD maps. As reference orientations the average orientation of the slices through the central RD–ND plane were chosen. The results for the three matrix orientations at 10% and 30% simulated rolling reduction are shown in Fig. 14. The GROD reaches maximum values of just below 10° at 10% simulated rolling reduction for all matrix orientations. At 30% rolling reduction the simulations show the highest GROD of about 17° for the $\langle 112 \rangle$ γ -fiber. The RC matrix is predicted to rotate away from the mean orientation by about 12.5 – 15° whereas the $\langle 011 \rangle$ γ -fiber barely exceeds GROD values of 12.5° . The simulation results are not fully consistent with the experimental findings. Possible reasons for the discrepancies are discussed in the next section.

In the CPFEM simulations the maximum accumulated crystallographic shear, i.e. the sum of the shear contributions on all slip systems, was observed on both sides of

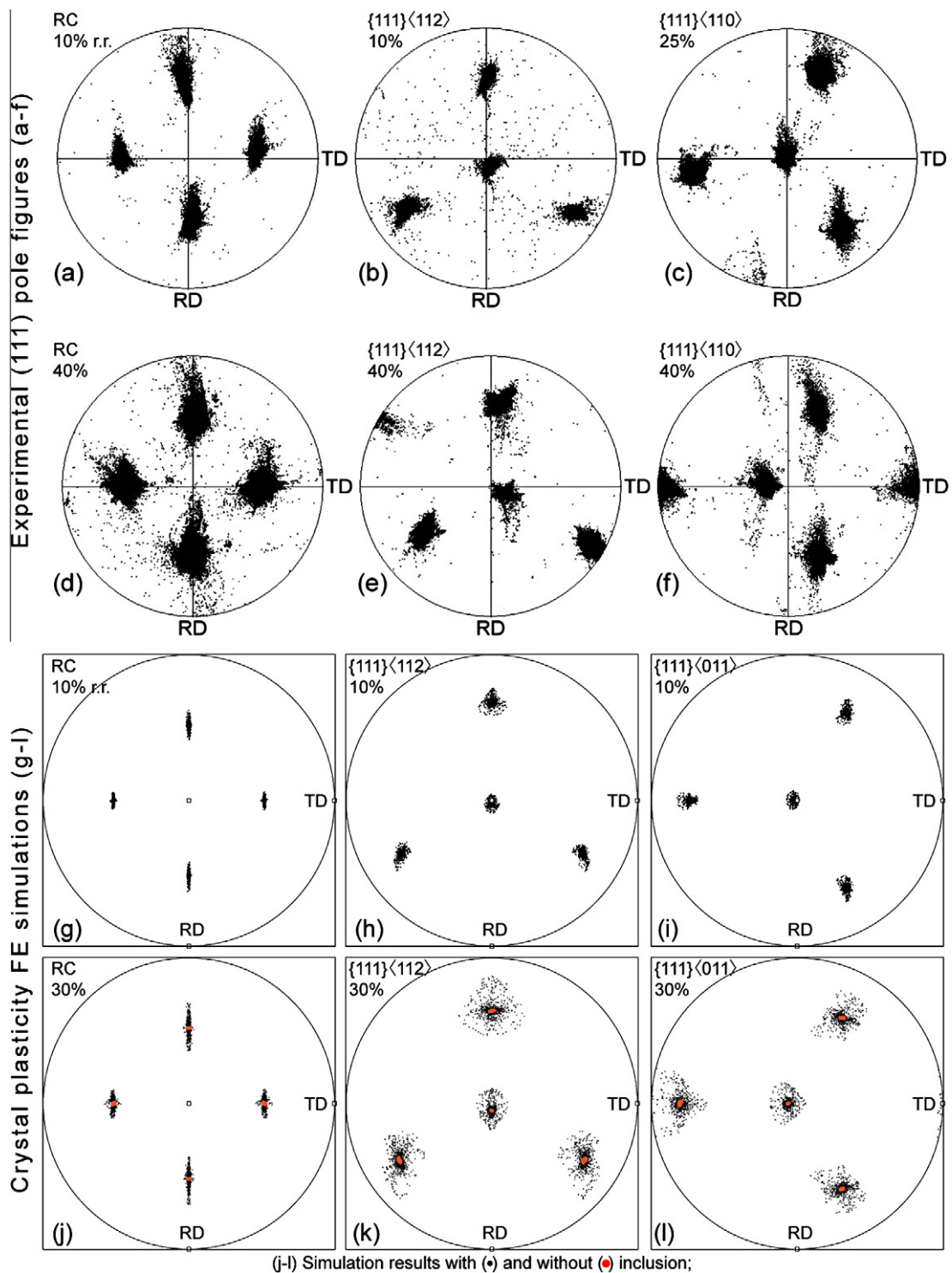


Fig. 12. Comparison of experimental (1 1 1) pole figures (a–f) and corresponding CPFEM predictions (g–l) at low (a–c, g–i) and high (d–f, j–l) amounts of rolling reduction. The experimental pole figures were obtained from $150 \times 150 \mu\text{m}^2$ areas inside large grains. For the simulated pole figures a random selection of 2000 discrete orientations is plotted. These orientations are not occupying the same volume of material but instead represent integration points of the finite-element mesh. In subfigures (j–l) the simulated texture evolution for an identical finite-element model for which the constitutive behavior was prescribed homogeneously (i.e. only matrix material without inclusion) is also shown by slightly larger red marks. (For interpretation of the references to color in this figure legend, the reader is referred to the web version of this article.)

the particle along the RD and ND directions. These zones of high slip activity deform predominantly in a uniaxial manner, namely in compression along the ND direction

above and below the particle, and by horizontal elongation on both sides of the particle along the RD direction. Between these zones, shear regions ensure material

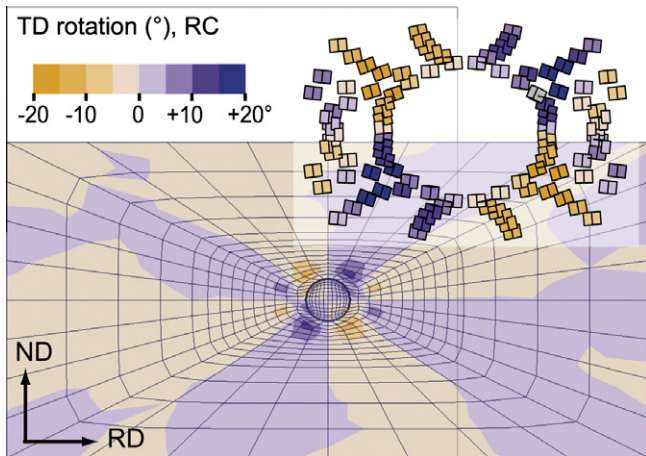


Fig. 13. Simulated lattice rotation about the TD-axis for a RC-oriented matrix at 30% rolling reduction. The inset magnifies the zones of maximum rotation depicted by one lattice cube per finite element.

continuity. Thus, the locations of the maximum unsigned values of the global RD–ND shear-strain component were observed in good agreement with the locations of the shear zones proposed above (Fig. 9), 45° away from the horizontal and vertical axes.

3.6. Discussion of the simulation results

In the simulations, the values of lattice rotations are averaged over the volume of the integration points of the finite elements. For the simulated problem, with the experimentally measured very high orientation gradients, the limited spatial resolution of the CPFEM mesh used becomes obvious. Hence, a fully quantitative treatment of the orientation gradients would require a much higher mesh resolution which is not possible at the moment owing to computational constraints.

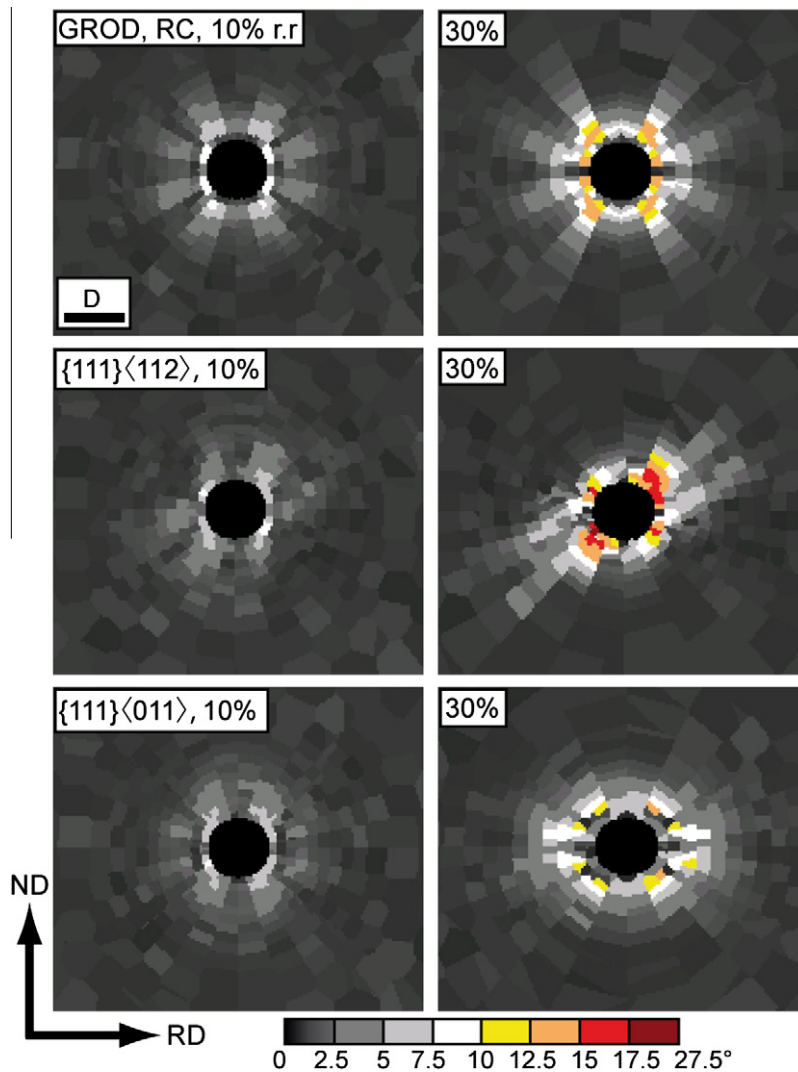


Fig. 14. Grain Reference Orientation Deviation (GROD) maps after 10% and 30% simulated rolling reduction. The colors correspond to the legend of Fig. 8 but scaled to one-half in terms of the corresponding rotation angles. (For interpretation of the references to color in this figure legend, the reader is referred to the web version of this article.)

The predicted GROD is of comparable magnitude and area fractions for all matrix orientations after 30% simulated rolling reduction. Several arguments could explain this deviation from the experimental findings where only limited lattice rotations occurred for the case of a γ -fiber matrix. One possible reason is that the chosen constitutive description might not capture the true non-linear hardening behavior of the material at the later stages of deformation. The work-hardening behavior for the high-temperature deformation conditions of the experiments might not have been represented accurately enough by the constitutive model because a considerable amount of dynamic recovery is assumed for the matrix material during, and especially in between, the warm rolling passes. Recovery mechanisms are not, however, included in the phenomenological material law used in the current simulations.

A second possible reason for the discrepancies between experiments and simulations might be that the local material model employed here might not be sufficiently accurate in a more fundamental sense because it does not take into account the additional hardening contributions from dislocation debris that might accumulate around the particle because of the impenetrable particle–matrix interface.

A third and quite important reason for the observed deviations is that the particle morphology can affect the formation of lattice rotations. The observed particle rotation for the case of a $\{111\}\langle 112\rangle$ matrix is probably not possible for the rod-shaped κ precipitates. Therefore, the particle shape could limit the lattice rotation around particles for matrix orientations close to $\{111\}\langle 112\rangle$ in the experiments. Consequently, the simulation would overestimate the orientation gradients around the particle for the $\langle 112\rangle$ γ -fiber matrix as it assumes a spherical shapes.

More detailed experimental and theoretical studies are necessary to finally decide which of these explanations is most plausible. A further observation from the CPFEM simulations might be helpful for future experiments: the computational results suggest that the experimentally performed analysis, based on sample cross-sections of the RD–ND planes, reveals the maximum effects of the lattice rotations for the matrix orientations RC and $\{111\}\langle 112\rangle$. In the case of a $\{111\}\langle 011\rangle$ matrix, cross-sectioning in the TD–ND plane was predicted to reveal the most active lattice rotation zones as also supported by the work of Konrad et al. [23].

4. Summary

Local lattice rotations and in-grain orientation gradients at κ precipitates in matrix grains with orientations near the 45° rotated cube $\{001\}\langle 110\rangle$ (RC) and the γ -fiber components $\{111\}\langle 112\rangle$ were investigated in a Fe₃Al alloy warm-rolled to reductions of between 10% and 60%. Corresponding CPFEM simulations on the idealized case of a spherical inclusion embedded in a bcc matrix assisted in the evaluation of the experimental data. The main results are:

- (1) Near-RC-oriented grains showed larger local lattice rotations at precipitates than γ -fiber grains. CPFEM simulation did not fully capture this behavior and possible reasons for the discrepancies were discussed.
- (2) In RC-oriented grains local lattice rotations could be described by a near-TD-rotation relative to the original grain orientation particularly at low reductions, and additional rotation components about the RD occurred at higher reductions. These findings were in good agreement with the corresponding CPFEM simulations.
- (3) In the γ -fiber grains the axes of the local lattice rotations were scattered between TD and RD. Absence of a predominant rotation axis in the case of γ -fiber was also observed in the CPFEM simulations.

References

- [1] Barrett CS, Levenson LH. *Trans Metall Soc AIME* 1940;137:112.
- [2] Beaudoin AJ, Mecking H, Kocks UF. *Philos Mag A* 1996;73:1503.
- [3] Raabe D, Zhao Z, Park SJ, Roters F. *Acta Mater* 2002;50:421.
- [4] Hu H. *Trans AIME* 1962;224:75.
- [5] Hu H. In: Himmel L, editor. *Recovery and recrystallization of metals*. New York: John Wiley and Sons; 1963. p. 311.
- [6] Dillamore IL, Morris PL, Smith CJE, Hutchinson WB. *Proc Royal Soc A* 1972;329:405.
- [7] Dillamore IL. In: Haessner F, editor. *Recrystallization of metallic materials*. Stuttgart: Dr. Riederer Verlag; 1984. p. 223.
- [8] Raabe D. *Phys Status Solidi (B)* 1994;181:291.
- [9] Raabe D. *Steel Res* 1995;66:222.
- [10] Raabe D, Schlenkert G, Weisshaupt H, Lücke K. *Mater Sci Technol* 1994;10:299.
- [11] Delannay L, Loge RE, Chastel Y, et al. *Adv Eng Mater* 2003;5(8):597.
- [12] Li SY, Van Houtte P, Kalidindi SR. *Model Simul Mater Sci* 2004;12(5):845.
- [13] Raabe D, Mao W. *Philos Mag A* 1995;71:805.
- [14] Raabe D, Keichel J. *Mater Sci Eng A* 1995;203:208.
- [15] Raabe D, Keichel J, Büscher M, Gottstein G. In: *Proceedings 16th RISØ int symp on mater science: materials, RISØ National Laboratory, Roskilde, Denmark; 1995*. p. 517–23.
- [16] Raabe D, Keichel J, Sun Z. *J Mater Sci* 1996;31:339.
- [17] Raabe D, Keichel J. *J Mater Res* 1996;11:1694.
- [18] Raabe D, Keichel J, Gottstein G. *Acta Mater* 1997;45:2839.
- [19] Kobayashi S, Zaefferer S, Schneider A, Raabe D, Frommeyer G. *Mater Sci Eng A* 2004;387:950.
- [20] Morris DG, Gutierrez-Urrutia I, Muñoz-Morris MA. *J Mater Sci* 2008;43:7438.
- [21] Kobayashi S, Zaefferer S, Schneider A, Raabe D, Frommeyer G. *Intermetallics* 2005;13:1296.
- [22] Kobayashi S, Zaefferer S. *Intermetallics* 2006;14:1252.
- [23] Konrad J, Zaefferer S, Raabe D. *Acta Mater* 2006;54:1369.
- [24] Kobayashi S, Zaefferer S, Raabe D. *Mater Sci Forum* 2007;550:345–50.
- [25] Kobayashi S, Zaefferer S. *Proc Mater Res Soc Symp Mater Res Soc* 2007;980. 0980-II01-03.
- [26] Kobayashi S, Takasugi T. *Intermetallics* 2007;15:1659.
- [27] Russell KC, Ashby MF. *Acta Metall* 1970;18:891.
- [28] Humphreys FJ. *Acta Metall* 1977;25:1323.
- [29] Humphreys FJ. *Acta Metall* 1979;27:1801.
- [30] Humphreys FJ, Kalu PN. *Acta Metall* 1990;38:917.
- [31] Humphreys FJ, Ardakani MG. *Acta Metall* 1994;42:749.
- [32] Ferry M, Humphreys FJ. *Acta Mater* 1996;44:3089.

- [33] Engler O. *Philos Mag A* 2001;81:543.
- [34] Clarke AP, Humphreys FJ, Bate PS. *Mater Sci Forum* 2003;426–432:399–404.
- [35] Schäfer C, Song J, Gottstein G. *Acta Mater* 2009;57:1026.
- [36] Ashby MF. *Philos Mag* 1966;14:1157.
- [37] Hölscher M, Raabe D, Lücke K. *Acta Metall* 1994;42:879.
- [38] Bate P. *Philos Trans Royal Soc London A* 1999;357:1589–601.
- [39] Humphreys J, Bate P. *Scripta Mater* 2003;48:173–8.
- [40] Kalidindi SR, Bronkhorst CA, Anand L. *J Mech Phys Solids* 1992;40(3):537–69.
- [41] Roters F, Eisenlohr P, Hantcherli L, Tjahjanto DD, Bieler TR, Raabe D. *Acta Mater* 2010;58(4):1152–211.